ON THE POSSIBILITY OF SIGNIFICANT ELECTRON DEPLETION DUE TO NANOGRAIN CHARGING IN THE COMA OF COMET 67P/CHURYUMOV-GERASIMENKO NEAR PERIHELION

E. VIGREN[1], M. GALAND[2], P. LAVVAS[3], A. I. ERIKSSON[1], AND J.-E. WAHLUND[1]
[1] Swedish Institute of Space physics, Uppsala, Sweden; erik.vigren@irfu.se
[2] Department of Physics, Imperial College London, London, UK
[3] Groupe de Spectrométrie Moléculaire et Atmosphérique, Université Reims Champagne-Ardenne, UMR 7331, F-51687 Reims, France

ABSTRACT

We approach the complicated phenomena of gas–dust interactions in a cometary ionosphere, focusing in particular on the possibility of significant depletion in electron number density due to grain charging. Our one-dimensional ionospheric model, accounting for grain charging processes, is applied to the subsolar direction and the diamagnetic cavity of 67P/Churyuomov-Gerasimenko, the target comet for the ESA *Rosetta* mission, at perihelion (∼1.25–1.30 AU). We argue on the one hand that grains with radii >100 nm are unlikely to significantly affect the overall ionospheric particle balance within this environment, at least for cometocentric distances >10 km. On the other hand, if nanograins with radii in the 1–3 nm range are ejected to the coma at a level of ∼1% with respect to the mass of the sublimated gas, a significant electron depletion is expected up to cometocentric distances of several tens of kilometers. We relate these results to the recent *Cassini* discoveries of very pronounced electron depletion compared with the positive ion population in the plume of Enceladus, which has been attributed to nanograin charging.

Key words: comets: individual (67P/Churyumov-Gerasimenko) – molecular processes

1. INTRODUCTION

Several plasma environments in the solar system, such as the D-region of Earth's ionosphere (e.g., Larsen et al. 1972; Thomas & Bowman 1985), Titan's deep ionosphere (e.g., Coates et al. 2007; Ågren et al. 2012; Shebanits et al. 2013; Lavvas et al. 2013; Wellbrock et al. 2013), the E-ring plasma disk of Saturn (Wahlund et al. 2005, 2009), and the plume of Enceladus (e.g., Morooka et al. 2011, Hill et al. 2012), host negative ions (including negatively charged grains), and therefore experience differences—sometimes pronounced—in the number densities of free electrons and positively charged ions. Such environments are subjected to *electron depletion*, resulting from important loss processes of free electrons beside the common dissociative recombination with positive ions. Whether the innermost ionospheres of active comets are also subject to pronounced electron depletion (due to dust charging) is still an open question. This question, anticipated to be answered by the ESA *Rosetta* mission en route to comet 67P/Churyumov-Gerasimenko (hereafter 67P), is addressed in the present modeling study.

Comet 67P, discovered in 1969, is a Jupiter-family comet with an effective radius of 2.04 ± 0.11 km (Kelley et al. 2009), an orbital period of ∼6.5 yr, and aphelion and perihelion distances of ∼5.7 AU and ∼1.25–1.30 AU, respectively. Following the rendezvous with 67P in 2014 August, *Rosetta* is set to follow the comet closely until the end of 2015 December. A lander (called *Philae*) will be delivered to the nucleus in 2014 November when the comet is at a heliocentric distance of ∼3 AU. Measurements by orbiter instruments near the perihelion passage in 2015 August are most highly relevant for the topic under consideration here. The (by then) well developed ionosphere in situ measurements by, e.g., the dual Langmuir probe (LAP; Eriksson et al. 2007), the Mutual Impedance Probe (MIP; Trotignon et al. 2007; two instruments of the *Rosetta* Plasma Consortium (RPC); Carr et al. 2007), and the

Rosetta Orbiter Spectrometer for Ion and Neutral Analysis (ROSINA; Balsiger et al. 2007) will provide the electron and ion number densities down to cometocentric distances of ∼5–20 km that will be critical for unraveling the importance of grains in the ionospheric particle balance. The presence and the charge density of negative ions can be revealed through the difference in number density of positive ions and free electrons. Note that there are also instruments on the orbiter that are devoted explicitly to dust analysis. The Cometary Secondary Ion Mass Analyzer (COSIMA; Kissel et al. 2007) will provide information on the composition of dust particles and the Grain Impactor Analyzer and Dust Accumulator (GIADA; Colangeli et al. 2007) will measure, e.g., the size, momentum, and velocity distribution of the dust grains (detection limit of ∼10 μm).

A series of observations during past perihelion passages shows that 67P is actively outgassing (mainly H_2O) with a molecular rate approaching 10^{28} s^{-1} (corresponding to ∼300 kg s^{-1}) a few weeks post-perihelion (e.g., Schleicher 2006; Tenishev et al. 2008; Snodgrass et al. 2013, Bertaux et al. 2014). Snodgrass et al. (2013) describe 67P as a dusty comet and estimate a perihelion dust mass production rate of ∼1000 kg s^{-1}, implying a substantial (>3) ratio in the dust-to-gas mass production rate (lower estimates, ranging from 0.21 to 1.5, have been made in the past; see Tenishev et al. 2011 and references therein). The bulk of the observed dust is in micrometer-sized and larger particles (see, e.g., Tozzi et al. 2011; Vincent et al. 2013; Snodgrass et al. 2013) and the activity is rather localized (e.g., Schleicher 2006; Lara et al. 2011; Snodgrass et al. 2013). Grains with radii much less than 0.1 μm are often ignored in descriptions of cometary grain size distributions (see Tenishev et al. 2011 and references therein) mainly because they have low scattering efficiency in the visible; therefore, they are difficult to observe from the ground. However, in the ionospheric particle balance, these grains may be of utmost importance. This is attested by, for instance, the pronounced level of electron depletion in the Enceladus plume. An electron to positive ion
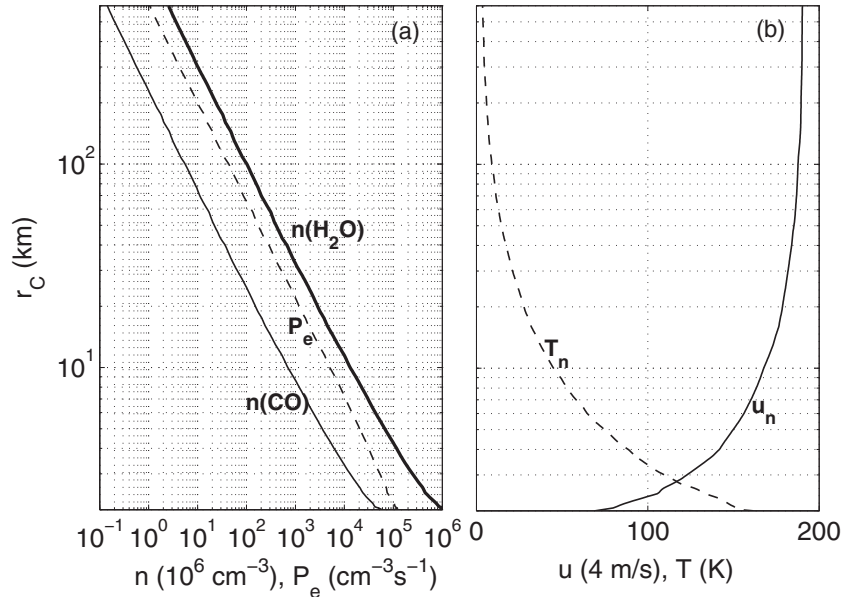
Figure 1. Neutral background and ionization rates considered in the model. Shown against the cometocentric distance r_C are (a) number densities of H_2O and CO (from Tenishev et al. 2008) with solid lines and the ion–electron pair production rate with a dashed line, resulting from ionization by primarily solar EUV photons but also from photoelectrons and their secondaries (from Vigren & Galand 2013), and (b) kinetic temperature (dashed line) and radial speed (solid line) of the neutral gas (from Tenishev et al. 2008).

number density ratio, n_e/n_i, that approaches values <0.05 has been observed there by the Radio Plasma Wave Science/ Langmuir probe (RPWS/LP) on board *Cassini* (Morooka et al. 2011). Such a ratio is partly attributed to nanograin charging as derived from *Cassini* Plasma Spectrometer/Electron Spectrometer (CAPS/ELS) observations of negatively charged nanograins with radii limited to a few nanometers (Hill et al. 2012).

Our aim in the present study is to *qualitatively* address the potential role of nano-dust (or grains) in the ionospheric particle balance within the innermost coma of 67P near perihelion. Our model, presented in Section 2, builds upon a pure gas-phase model (Vigren & Galand 2013) and is applied to the sub-solar direction and the diamagnetic cavity of the cometary coma into which solar wind particles have no access. The location of the diamagnetic cavity surface of 67P has been estimated to be at ~30 km on the sunlit side at perihelion (Hansen et al. 2007), but the exact location (which will be revealed by the Flux Gate Magnetometer (MAG) on *Rosetta*; Glassmeier et al. 2007) is expected to be highly variable with solar wind conditions and outgassing rates. Therefore, results, presented and discussed in Section 3, are shown for cometocentric distances extending to 600 km. Conclusions are given in Section 4.

2. MODEL

2.1. Model Description

We numerically solve a set of coupled continuity equations accounting for ion–electron pair formation, transport of species radially outward, ion–electron dissociative recombination reactions, and grain charging/neutralization through photoprocesses as well as through electron and ion attachment to the grains. The neutral background, shown in Figure 1, is taken from Tenishev et al. (2008) and includes the profiles of H_2O and CO number densities, neutral kinetic temperature, and radial speed versus cometocentric distance, r_C. The total ion–electron pair production rate, $P_e(r_C)$, from photoionization and electron

impact ionization under solar illumination is taken from Vigren & Galand (2013) and is shown with a dashed line in Figure 1(a). The plasma velocities and the plasma temperature are set according to the neutral background in the simulations (see further Section 2.2) unless otherwise stated.

The species considered in the model are electrons (e), gasphase positive ions (i), and grains (G) of radius a_{eff} and mass density $\rho = 1$ g cm^{-3}. The grains are further labeled by their charge state, e.g., G_0 and G_{-4} for grains in charge states 0 and -4, respectively. In each simulation, grains of one single fixed size are considered. As our focus is not on the details of the ion composition, the gas-phase ion population is treated as only containing ions with a mass of 19 amu (the mass of H_3O^+). This simplification removes the computational burden of modeling a detailed ion–neutral chemistry scheme. Besides, when using a dissociative recombination rate coefficient of $k_{ei} = 7.6 \times 10^{-7} \times (T_e/300)^{-0.83}$ cm^3 s^{-1} (based on experimental studies on the DR of H_3O^+ by Neau et al. 2000) and ignoring the grains, the associated model run yields an electron number density profile that is similar to within 10% for $r_C < 600$ km to that derived in Vigren & Galand (2013), who include a multi-component ion-chemistry accounting for 11 ion species including species with a higher proton affinity than that of H_2O.

The electron and ion attachment processes to the grains (e.g., $e + G_{-4} \rightarrow G_{-5}$; $i + G_{-2} \rightarrow G_{-1}$) are given rate coefficients according to analytical expressions of Draine & Sutin (1987):

$$k_{xG} = S_x \sqrt{\frac{8k_B T_x}{\pi m_x}} \pi a_{eff}^2 J(\upsilon, \tau), \tag{1}$$

where S_x, T_x, and m_x are the coefficient, kinetic temperature, and mass of species x ($x = e$ or i), k_B is Boltzmann's constant, a_{eff} is the grain radius, and J is a parameter that depends on υ, the ratio of the charge on the grain to the charge of the incident particle and the reduced temperature, τ, which is given by:

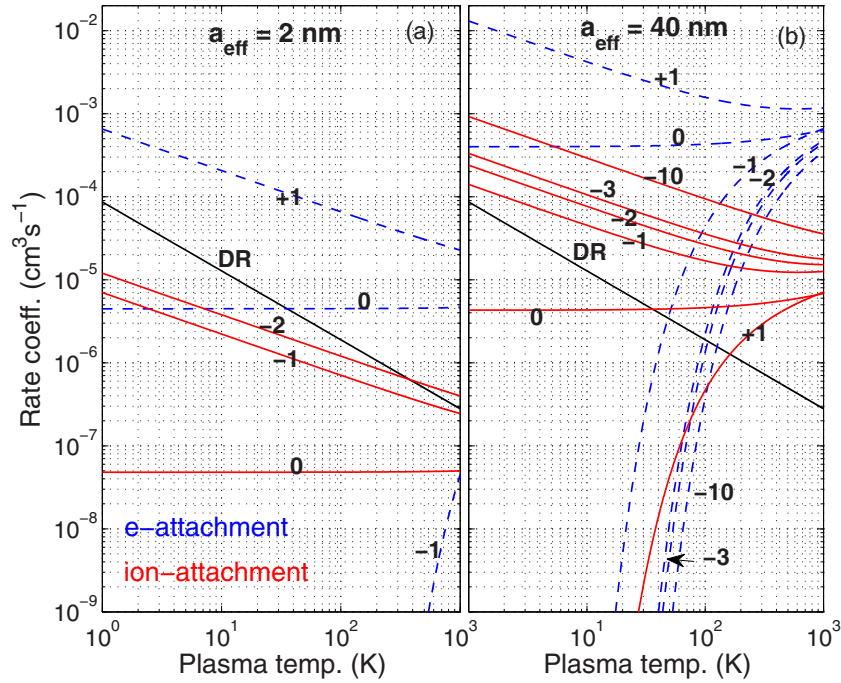$$\tau = \frac{4\pi \varepsilon_0 k_B a_{eff} T_x}{q_x^2}, \tag{2}$$

Figure 2. Rate coefficients as a function of electron temperature (ion temperature) for the attachment of electrons (ions) to grains in indicated charge states and of radii: (a) 2 nm, and (b) 40 nm. The blue dashed lines are electron attachment curves while the red solid lines are ion attachment curves. The rate coefficients are based on the formalism by Draine & Sutin (1987). We have assumed electron and ion sticking coefficients of 0.5 and 1.0, respectively, and an ion mass of 19 amu. The solid black line represents the dissociative recombination rate coefficient as a function of electron temperature experimentally derived for H_3O^+ (Neau et al. 2000).

where ε_0 is the permittivity constant and q_x the charge of the particle impinging the grain. For neutral ($\upsilon = 0$), attracting ($\upsilon < 0$), and repelling ($\upsilon > 0$) grains:

$$J(\upsilon, \tau) = \begin{cases} 1 + [\pi/(2\tau)]^{1/2} & \upsilon = 0 \\ (1 - \upsilon/\tau) \times (1 + [2/(\tau - 2\upsilon)]^{1/2}) & \upsilon < 0 \\ [1 + (4\tau + 3\upsilon)^{-1/2}]^2 \\ \quad \times \exp[-\upsilon/(\tau + \tau\upsilon^{-1/2})] & \upsilon > 0 \end{cases}$$

(3)

The sticking coefficients are set (based, e.g., on the work by Weingartner & Draine, 2001) to conservative values of 0.5 for electrons and 1.0 for ions. We stick to these values regardless of the charge state and size of the grains, and regardless of the temperature of the ions and the electrons. Examples of rate coefficients for attachment processes of ions and electrons to grains of different sizes and charge states are given in Figure 2.

We denote the unattenuated photoelectron emission rate from uncharged grains (i.e., for the process $G_0 + h\nu \rightarrow e + G_{+1}$) by $k_{G(h\nu)}$ and estimate its value based on, e.g., Horányi (1996):

$$k_{G(h\nu)} = \pi a_{eff}^2 \times 2.5 \times 10^{14} \kappa/d_{AU}^2, \quad (4)$$

where $k_{G(h\nu)}$ is in unit s^{-1} of when the grain radius a_{AU} is inserted in meters and the heliocentric distance, d_{AU}, is inserted in AU. The dimensionless parameter κ is an efficiency factor close to 1 for conducting material and close to 0.1 for dielectric material. We set $\kappa = 0.1$ as a default value in our simulations suitable, e.g., for ice (see Hsu et al. 2013; Meyer-Vernet 2013; Mann et al. 2014). We modify the photoionization frequency of the grains at low r_C to account for attenuation of the ionizing solar irradiation. This is done through the assumption that the photoionization frequency of a grain at a particular cometocentric distance

is proportional to the photoionization frequency of an ambient gas-phase molecule. The latter parameter is shown against r_C in Figure 5(c) of Vigren & Galand (2013). It shows that the attenuation effect becomes significant only below ~20 km. We ignore photoelectron emission from positively charged grains as such grains are anticipated to rapidly (in relation to the timescale for the photoionization) collect free electrons. The right-hand side of Equation (4) is also used as the rate for the photodetachment of electrons from negatively charged grains (e.g., $G_{-1} + h\nu \rightarrow e + G_0$ and $G_{-3} + h\nu \rightarrow e + G_{-2}$; see Horányi 1996; Hsu et al. 2013; Mann et al. 2014), a treatment that can be questioned (from the intuition that the more negatively charged a grain is, the less energy is required to remove an electron from it). We discuss its validity in Section 3.2. The rates utilized for the photoprocesses of the grains are highly uncertain (note, for example, that Equation (4) does not account for solar conditions with variations in the EUV by >100% over a solar cycle). This does not add large uncertainties to our principal model results because, for the small grains considered, and within the simulated environment, the described photoprocesses are of less importance than the ion attachment on grains (see the sensitivity tests in Section 3.2).

In the simulations, the grains are ejected uncharged from the surface. The grain mass-loss rate from the surface (in the subsolar direction) is set to a fraction M^* of the gas mass-loss rate, with the gas mass-loss rate derived from the H_2O and CO data provided in Tenishev et al. (2008). In the vicinity of the surface, the number density n of grains G_Z of charge state Z is related to M^* via

$$M^* \approx \frac{m_G \sum_z n(G_Z)}{n(H_2O)m(H_2O) + n(CO)m(CO)}, \quad (5)$$

where n and m denote number densities and masses, respectively, and where the sum in the numerator is over grains in different

charge states with each grain assumed to be spherical and therefore having a mass m_G, given by:

$$m_G = \frac{4\pi a_{eff}^3 \rho}{3},\tag{6}$$

where a_{eff} and ρ are the radius and mass density of a grain.

2.2. Simplifying Aspects

Applying our model to the diamagnetic cavity avoids some complicating aspects in the modeling such as the ionization by solar wind particles and the transport of charged species along magnetic field lines. Still, several simplifications have been made, which are mainly justified by our qualitative aims, and which are presented in Sections 2.2.1–2.2.3 for transparency.

2.2.1. Grain Treatment

For a given run, a single grain size is considered instead of a grain size distribution. We treat the grains as spherical, nonfragmenting, noncoagulating (justified by the low pressure and the rapid transport radially outward), and, when entering the coma, exclusively uncharged. For the grain charging processes, we apply in each simulation electron and ionsticking coefficients that do not vary with the charge state of the grains. In Section 3.2, we investigate how changes in the electronsticking coefficient affect modeling results. Also, related to our treatment of the grain charging, we do not account for screening effects by surrounding charged grains, but use the same formalism/ equations (from Draine & Sutin 1987) regardless of the model scenario. In some simulations, the grains are "isolated" with the intergrain distance exceeding the local Debye length, while in other simulations the opposite relation prevails ("dusty plasma" instead of "dust-in-plasma"). Goertz & Ip (1984) showed that the charge of a grain in a dusty plasma is reduced with respect to its free space value. That is, as outlined in, e.g., Mendis & Horányi (2013), due to the depletion of free electrons required by the charge neutrality condition $n_i - n_e = -Zn_G$, which can result in $n_e \ll n_j$, implying that the difference between the surface potential of a grain and the ambient plasma potential does not need to be as negative as in the case of an isolated grain for the electron and ion currents to the grain to balance. While the charge neutrality condition is applied in our calculations (further limiting the number of excess electrons the grains can carry), we do not account for the increased grain-to-plasma capacitance occurring when the grain's Debye spheres overlap (Whipple et al. 1985). Note, however, that the increase in grain-to-plasma capacitance due to neighboring grains is negligible as long as the grain size is *much* smaller than the intergrain distance and the Debye length (see Whipple et al. 1985; Meyer-Vernet 2013), which is the case in all of our simulations (see Section 4).

2.2.2. Radial Transport Only

We make no attempt to account for the localized activity of the comet. The transport terms in our continuity equations only take into account motion radially outward. We assume the electrons, the gas-phase ions, and the grains (regardless of size or charge state) to move radially outward with the same speed as that of the bulk gas shown in Figure 1(b). For the ions and the electrons, and within the diamagnetic cavity, this is likely a reasonable approximation (see, e.g., Körözmezey et al. 1987). For the grains the assumption seems justified for small sizes, i.e., with radii near or less than $\sim$100 nm (see, e.g., Davidsson

et al. 2010; Tenishev et al. 2011; Fink & Rubin 2012), which is the range at which we primarily focus here. In Section 3.2, we make sensitivity tests on how modeling results are affected by reducing the outward radial speed of all species by a factor of two.

2.2.3. Plasma Temperature

We assume the ion and electron populations to be characterized by isotropic Maxwellian speed distributions in the frame of the bulk gas/dust ensemble moving radially outward. We set the electron and ion temperatures (T_e and T_i) equal to each other and equal to the neutral temperature (T_n) shown in Figure 1(b). The $T_e = T_n$ assumption is motivated in part by the fact that H_2O is an efficient electron coolant (see, in particular, Cravens & Körözmezey 1986) and that the simulations are only intended for the diamagnetic cavity. In Sections 3.1.2 and 3.2, we make sensitivity tests in order to explore how the model results are affected by considering higher plasma temperatures. Note that the neutral temperature profile is not a priori a direct input to the model; it indirectly affects the results due to the assumption that the plasma temperature is governed by T_n. Therefore, model runs with increased plasma temperatures can be regarded as covering scenarios either with (1) plasma temperatures elevated above the neutral temperature, or (2) higher neutral temperatures than in the default model inducing higher plasma temperatures.

3. RESULTS AND DISCUSSION

3.1. R1–R4 Simulations

In the model runs, we explore in particular how different values of a_{eff} (the grain radius) and M^* (the dust-to-gas mass emission ratio) affect the overall ionospheric particle balance. Four case studies, labeled R1–R4, are considered initially with (a_{eff}, M^*) parameters of (200 nm, 1), (100 nm, 1), (40 nm, 0.5), and (2 nm, 0.01), respectively. The results from the model runs are shown in Figure 3. In each panel, we also show for comparison the total ion number density (equal to the electron number density) calculated in the pure gas-phase model (with $M^* = 0$).

3.1.1. Grains with Radii >100 nm, the R1 and R2 Simulations

From Figures 3(a) and (b), we raise the hypothesis that grains with radii >100 nm are unlikely to have a profound influence on the overall ionospheric particle balance within the diamagnetic cavity of 67P. As for the R2 results seen in Figure 3(b), the calculated n_e values are >15% lower than values from the pure gas-phase model within only $\sim$4 km from the surface. Going from R2 to R1 (from Figures 3(b) to (a)), the number density of the grains decreases, but the larger grains can carry more excess electrons. The combined effect is a reduced influence on the overall ionospheric particle balance with the n_e and n_i profiles being essentially inseparable from the results from the pure gas-phase model. In both the R1 and R2 simulations, we use $M^* = 1.00$. In Section 1, we mentioned, on the one hand, that the dust mass production rate of 67P may be higher than the gas mass production rate by a factor of a few (near perihelion), but, on the other hand, that the bulk of the dust mass is in micrometer-sized and larger particles. The second point suggests that M^* values of 1.00 may be unrealistically high for grains with radii in the vicinity of $\sim$0.1 microns. To this end, it is noted that for the subsolar direction and perihelion, Tenishev et al. (2011) calculate at $r_C = 20$ km a number density less than 3 cm^{-3} for
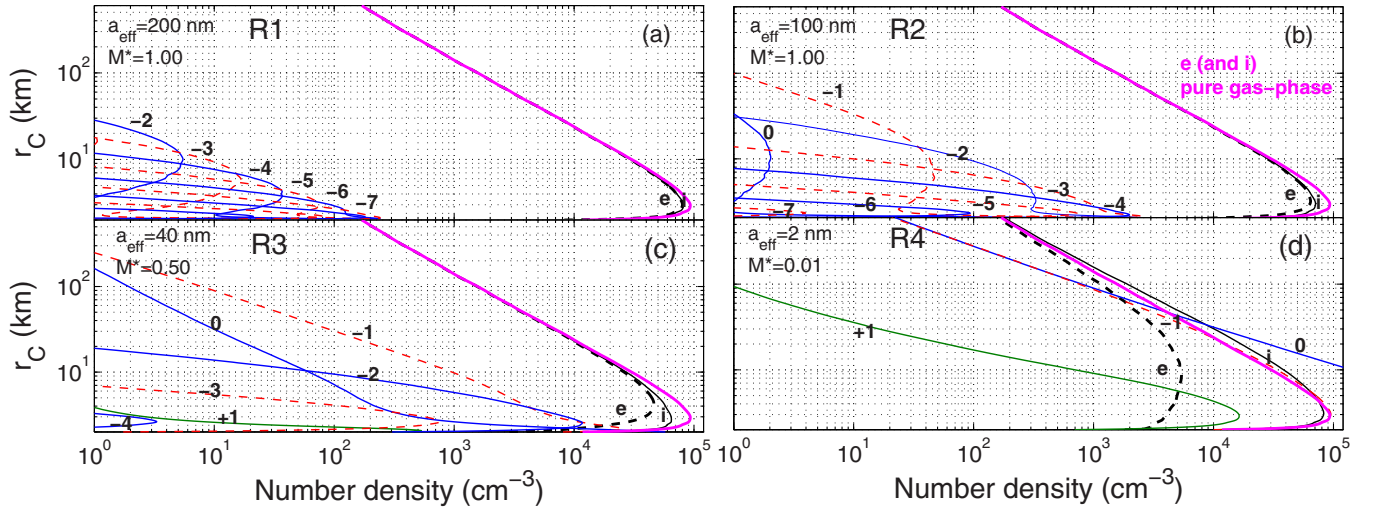
Figure 3. Calculated number densities of species vs. cometocentric distance. Positively charged grains are shown by green lines, while the other grains are displayed by blue solid lines (red dashed lines) when in an even (odd) charge state. The bold dashed black line shows the electron number density and black solid line shows the number density of gas-phase positive ions. The bold magenta line shows the electron number density calculated in a pure gas-phase model. The different panels correspond to model runs with different a_{eff} and M^* values (see the text). The e and i lines in panel (a) and (coincidentally) the G_{-1} and G_0 lines in panel (d) for cometocentric distances exceeding 65 km are difficult to separate.
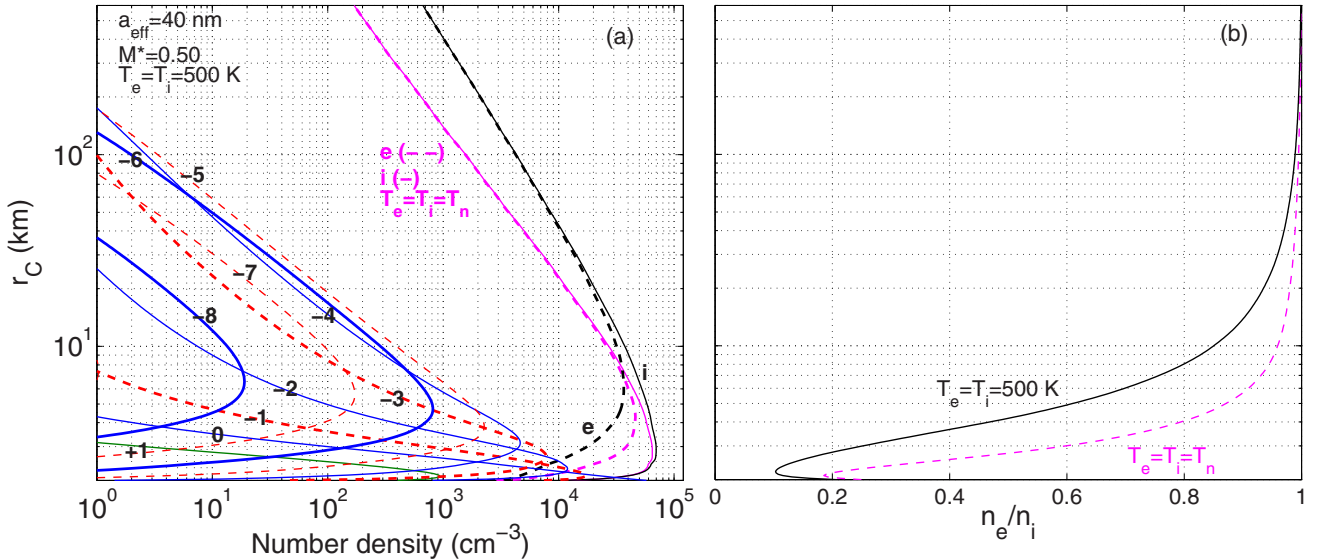

Figure 4. (a) Calculated number densities of species vs. cometocentric distance from a model run using a constant plasma temperature of 500 K. The green line shows positively charged grains, while the other grains are displayed by blue solid lines (red dashed lines) when in an even (odd) charge state. The bold, dashed black line shows the electron number density, and the black solid line shows the number density of gas-phase positive ions. The magenta lines are results from R3, a simulation similar except with the plasma temperature set equal to the neutral temperature (Figure 1(b)), and the corresponding charge state distribution of the grain population is shown in Figure 3(c). (b) Calculated n_e/n_i ratios for the two different model runs.

grains with radii 100–150 nm (see their Figure 9(a)), while in the R2 simulation the number density of the 100 nm grains at the same cometocentric distance is $\sim$25 cm^{-3}.

3.1.2. The R3 Simulation and the Effect on Charge State Distributions of Increased Plasma Temperature

Figure 3(c) shows results from the R3 simulation (with grains of radius 40 nm ejected at an M^* level of 0.50). A difference in electron number density compared with the pure gas phase simulation (magenta curve) is clear only for cometocentric distances less than $\sim$10 km. For even lower r_C, the level of electron depletion becomes quite substantial with the n_e/n_i ratio reaching a minimum of $\sim$0.2 in the very vicinity of the surface.

We stick with R3 to illustrate the sensitivity of the ambient plasma temperature on the charge state distribution of the grains. In Figure 4, we show results from R3 adjusted with $T_e = T_i$ set

to a constant value of 500 K (to be regarded as a high value well inward of the diamagnetic cavity surface).

As seen by comparing Figure 4(a) with Figure 3(c), the increased plasma temperature changes drastically the charge state distribution of the grains. Furthermore, an increase in the electron number density is seen for $r_C > 10$ km as the plasma neutralization through dissociative recombination becomes less efficient with increased T_e (see Figure 2). In Figure 4(b), we show how the increased plasma temperatures affect the n_e/n_i ratio. The ratio decreases with increased temperature, as the grains can collect more excess electrons in a hotter plasma surrounding. Nevertheless, the level of electron depletion becomes substantial only for $r_C < 10$ km, where collisions with the gas-phase surrounding are anticipated to rapidly thermalize the electrons and ions to the neutral temperature. Setting M^* to 1.00 instead of 0.50 in the R3 run, the n_e/n_i ratio at 10 km (20 km)
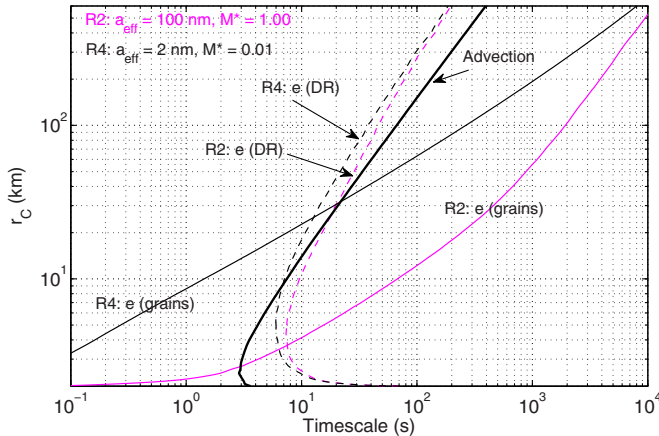
Figure 5. Timescales vs. cometocentric distance for the R2 and R4 simulations. The solid lines labeled "e(grains)" show the expected lifetimes of a free electron to attach to a grain. The dashed lines labeled "e(DR)" show electron lifetimes against loss through dissociative recombination with positive ions. The thick black line shows the timescale for advection, $t_{adv} \sim r_C \times (2u)^{-1}$.

becomes equal to 0.92 and 0.68 (0.96 and 0.85) in the $T_e = T_i = T_n$ and the $T_e = T_i = 500$ K cases, respectively.

3.1.3. The Results from R4 versus Those from R1 and R2

In R4 $a_{eff} = 2$ nm and $M^* = 0.01$ and the results of the model run, displayed in Figure 3(d), are striking at first sight. Electron depletion is clearly present even for $r_C > 100$ km and the ratio $n_e/n_i < 0.5$ for $r_C < 65$ km. The main reason why the grains in R4 have a much more pronounced influence on the ionospheric particle balance than the grains in R2 (where $a_{eff} = 100$ nm and $M^* = 1.0$) is because, for any given r_C, they prevail in a number density 1.25×10^3 times higher (compare the M^*/a_{eff}^3 ratios). In addition, the larger grains in R2 rapidly reach a charge state where electron and ion currents balance. As an example, a few kilometers above the surface where the model plasma temperature is ~100 K, the R2 grains are predominantly in the charge states -3 and -4 and the effective electron attachment rate coefficient is only about a factor of 10 higher than the corresponding effective rate coefficient for attachment to the R4 grains of radius 2 nm, which are predominantly neutral (the nanograins considered in R4 are too small to carry more than one excess electron and this holds even when increasing the plasma temperature to a constant value of 500 K). Combined, this makes the timescale for electron loss through grain attachment about two orders of magnitude higher in R2 than in R4 as seen (for $r_C < 10$ km) in Figure 5.

We note also from Figure 5 that in R4 (R2) the timescale for electron attachment to grains is less than the advection timescale—as given by $t_{adv} \sim r_C \times (2u)^{-1}$—for r_C less than ~30 km (~3 km). In R4, $r_C \sim 30$ km is also the limit above which dissociative recombination becomes more important than attachment to grains in the removal of free electrons from the gas phase.

3.2. Nanograin Simulations and Sensitivity Tests

In Table 1, we show the r_C values below which $n_e/n_i < 0.5$ for a selection of simulations involving nanograins with a_{eff} ranging from 1 nm to 10 nm and with M^* ranging from 0.001 to 0.1. The picture that emerges is that *if* nanograins, with radii in the 1–3 nm range, are ejected to the coma at a level of 1% (or more) with respect to the mass of the ejected

Table 1
Cometocentric Distance Below Which $n_e/n_i < 0.5$ for Different Combinations of a_{eff} and M^*

$a_{eff} \backslash M^*$	0.001	0.005	0.01	0.05	0.1
1 nm	32 km	180 km	360 km	>600 km[a]	>600 km[b]
2 nm	6 km	30 km	65 km	340 km[c]	>600 km[d]
3 nm	(0.53)	10 km	22 km	120 km	230 km[e]
5 nm	(0.77)	3.5 km	6 km	28 km	58 km
10 nm	(0.93)	(0.73)	(0.54)	5 km	8 km

Notes. Values within parentheses are the lowest n_e/n_i ratio encountered in runs where $n_e/n_i > 0.5$ for all r_C.
[a] $n(G_{+1}) > n_i$ for $r_C < 20$ km.
[b] $n(G_{+1}) > n_i$ for $r_C < 50$ km.
[c] $n(G_{+1}) > n_i$ for $r_C < 6$ km.
[d] $n(G_{+1}) > n_i$ for $r_C < 12$ km.
[e] $n(G_{+1}) > n_i$ for $r_C < 5$ km.

gas, a significant level of electron depletion is expected for cometocentric distances of several tens of kilometers, possibly even throughout the diamagnetic cavity. Significantly higher emission levels of nanograins from the surface are required to markedly reduce the number density of the gas-phase positive ions (see notes in Table 1). In fact, the n_i values in R4 are even somewhat higher than in the pure gas-phase model for $r_C > 4$ km. This is due to the fact that the ions react more slowly with the negatively charged nanograins of radius 2 nm than with free electrons, as seen in Figure 2(a). Thus, as electrons attach to the 2 nm nanograins, the positive ions become longer-lived.

We have explored how the results of the simulations are changed by adjustments of various input parameters. Increasing (decreasing) the grain mass density ρ from the default value of 1.0 g cm^{-3} to a different value has exactly the same effect as decreasing (increasing) M^* by the same factor. Thus, if the R4 simulation is adjusted to consider, e.g., grains of density 2.0 g cm^{-3} (instead of 1.0 g cm^{-3}), the cometocentric distance below which $n_e/n_i < 0.5$ becomes approximately 30 km (instead of ~65 km), as shown in Table 1.

Increasing the rate for the photodetachment (from negatively charged grains) by 50% in R4 has a very minor influence on the resulting number densities and electron depletion level. The increase in the n_e/n_i ratio is less than 0.5% for all r_C. The effects on the R4 results of considering rates 30 times higher for electron removal from grains by photons and by using an electron sticking coefficient, S_e, of only 0.2 instead of 0.5 are shown in Figure 6. The effect of the increased photoemission rate is more pronounced at higher r_C while the reduced S_e markedly changes the results for all r_C. Incorporating both of the adjustments results in a clear reduction in the level of electron depletion, though still $n_e/n_i < 0.5$ for $r_C < 30$ km.

Reducing by a factor of two the outward radial speed of all species (keeping all other input parameters of R4 fixed, including the number density profiles of H_2O and CO) only has a minor influence on the model results. The resulting n_e/n_i ratio (not shown) is lower than in the default R4 simulation by ~30% at $r_C = 5$ km and by less than 10% for $r_C > 15$ km. The somewhat enhanced level of electron depletion follows from the fact that the grains (before reaching a particular cometocentric distance) are given a longer time to collect charges.

Finally, sensitivity of the results under R4 conditions with plasma temperature has been tested (see Figure 7). Increasing the plasma temperature to $T_e = T_i = 500$ K makes the neutralization of negatively charged grains by ion collection much less
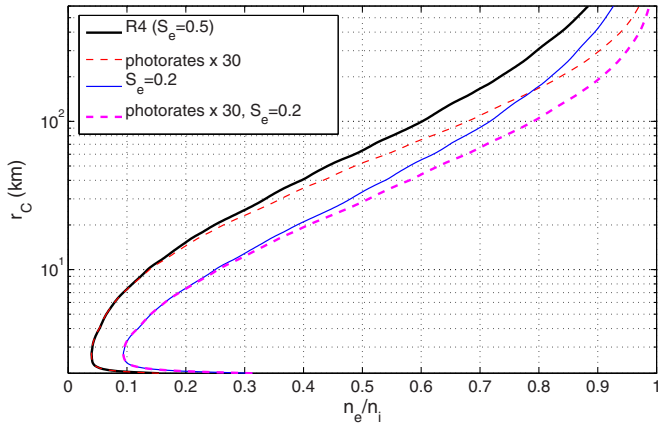
Figure 6. n_e/n_i ratio vs. cometocentric distance for the R4 simulation (black line) and for simulations similar to R4 but with the photoelectron emission rates from the grains increased by a factor of 30 (red dashed line) and the electron sticking coefficient to the grains set to 0.2 (blue line). The dashed magenta line shows the results when both changes are implemented for the same simulation.
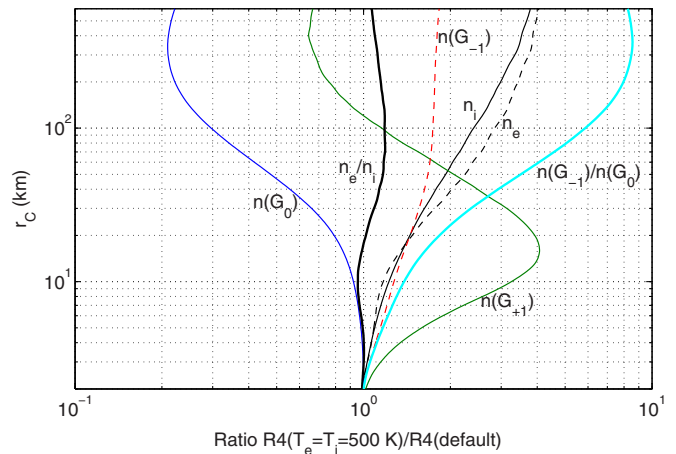

Figure 7. Effects on the R4 simulation results of setting $T_e = T_i = 500$ K instead of having the plasma temperature set according to the neutral temperature profile shown in Figure 1(b). The increased electron and ion number densities (dashed and solid black lines, respectively) follow from the decreased efficiency of dissociative recombination with increased plasma temperature. With fewer electrons and ions lost through recombination, the number density of neutral grains (blue line) decrease due to enhanced charging, which also gives increased number densities of negatively charged grains (red dashed line) and an increased $n(G_{-1})/n(G_0)$ ratio (cyan line). The effects on the number density of positively charged grains is shown by the green solid line while the effects on the n_e/n_i ratio is seen by the bold black line.

effective, so that $n(G_{-1})$ exceeds $n(G_0)$ by more than a factor of three for $r_C > 100$ km as contrasted by the results from the default R4 simulation where $n(G_0)$ and $n(G_{-1})$ are similar to within 20% for 65 km $< r_C <$ 600 km. Increasing T_e also means a reduction in the importance of ion–electron dissociative recombination (see Figure 2). This yields an increase in the overall plasma number density. Associated with the fact that very small grains considered in R4 cannot carry more than a single excess electron, this means that the increased plasma temperatures slightly decreases the r_C below which $n_e/n_i < 0.5$ to a value of ~50 km instead of ~65 km.

3.3. Is it Realistic with $M^* = 0.01$ for Nanograins with Radii <3 nm?

Despite estimates on the total dust emission rate of 67P-CG at perihelion (see Section 1), it is difficult to set constraints on the ejection rate of nanograins from the surface and the amount of nanograins present in the coma. Measurements in the very extensive coma of comet Halley by the ion mass spectrometers onboard Giotto and the two Vega space missions led Utteback & Kissel (1990) to estimate that attogram grains (within a distance of half-million kilometers from the nucleus) accounted for several percent of the total mass loss (see also Sagdeev et al. 1989). High number densities of such very small grains at large distances from a cometary nucleus do not, however, necessitate their rich presence in the surrounding near nucleus owing to the possibility of formation via the fragmentation of larger grains. Observations indicative of significant fragmentation of grains in cometary comae are presented in, e.g., Utteback & Kissel (1990) and Konno et al. (1993).

The sources (and the mechanisms behind the formation) of the Enceladus plume and the coma of 67P-CG are likely very different. While a cometary coma results from solar heating and sublimation at the surface and near surface layers, the plume likely emerges from water vapor venting from subsurface reservoirs of liquid water (Porco et al. 2006). It is possible that the grain populations carried aloft by the gas in these environments differ substantially in terms of size distribution, composition, and morphology. Still, it is interesting to note that the a_{eff} values and the M^* values in the R4 simulation of 67P in fact seem to be in line with "nanograin parameters" in the Enceladus plume. First, spectra recorded by the

CAPS/ELS and the CAPS/Ion Mass Spectrometer (IMS) onboard the *Cassini* spacecraft during the Enceladus E3 and E5 encounters display signs of maximum count rates near the instrumental upper energy limit (~30 and ~34 keV charge^{-1} for ELS and IMS, respectively). Taking into account the spacecraft velocities during the encounters and assuming singly charged spherical grains with a density of water ice, the corresponding grain radii at the upper energy limit is ~2 nm (Hill et al. 2012). Second, the in situ measurements by the CAPS/ELS and the Ion & Neutral Mass Spectrometer (INMS) during the E3 encounter by *Cassini* Hill et al. (2012) showed that the mass of negatively charged nanograins with radii <2.2 nm (radius derived from assumptions of spherical grains and density of water ice) was ~1% of the water gas mass in parts of the trajectory through the plume (see their Figure 9). On the one hand, the CAPS/ELS does not measure the uncharged nanograins, suggesting the fraction of nanograins to be even larger (unless all nanograins are negatively charged). On the other hand, it cannot be ruled out that the charged nanograins observed during the Enceladus flybys may have formed in part through the fragmentation of larger particles.

4. CONCLUSIONS

We have presented a model with gas–dust interactions mainly to qualitatively address the possibility of significant electron depletion within the diamagnetic cavity of comet 67P/ Churyumov-Gerasimenko near perihelion (1.25–1.3 AU). While we have relaxed the gas-phase ion-chemistry scheme compared with Vigren & Galand (2013), we have introduced grains to the simulated ionospheric particle balance. In our simulations, the grains are treated as leaving the surface uncharged, thereafter traveling radially outward with the same radial speed as that of the bulk gas. The utilized rate coefficients for the key attachment processes to grains are based on Draine & Sutin (1987) and take into account grain polarizability effects, effectively making the electron attachment and ion attachment to neutral grains
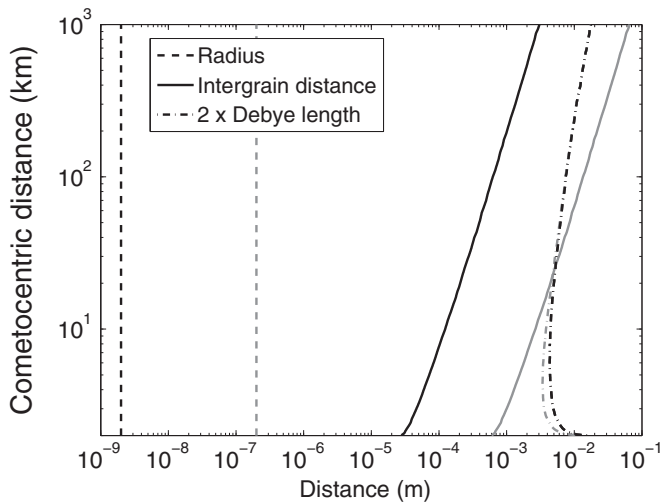
Figure 8. Shown vs. cometocentric distance are the grain radius (dashed), integrain distance (solid), and twice the Debye length (dash-dotted) associated with the R1 (gray) and R4 (black) simulations. The R1 (R4) simulation is associated with 200 nm grains and $M^* = 1.00$ (2 nm grains and $M^* = 0.01$).

proceed with roughly constant rate coefficients at sufficiently low temperatures (see Figure 2).

Several simplifications have been implemented (see in particular Section 2.2) and we wish to stress that the simulations are intended for a "perfect" diamagnetic cavity where solar wind particles have no access. For any given simulation, we consider grains that are identical in shape (spherical), density (1 g cm^{-3}), and size. The two key findings of our study are as follows.

1. Grains with radii >100 nm are unlikely to contribute significantly to a high level of electron depletion within the diamagnetic cavity, especially for cometocentric distances exceeding 10 km.
2. If the mass of nanograins with radii in the 1–3 nm range is at the level of ~1% (or more) with respect to the mass of the gas in the near nucleus surrounding, a significant level of electron depletion, with n_e/n_i ratios <0.5, is expected up to cometocentric distances of several tens of kilometers, possibly throughout the diamagnetic cavity.

The second statement is supported by a series of sensitivity tests where input parameters of the "nanograin simulations" have been changed, but where the principal result (a high level of electron depletion in the innermost coma) remains. An important follow-up question associated with the second statement is whether it is realistic with such a "high" presence of nanograins. This was discussed in Section 3.3 with references to in situ observations both in the very extended coma of comet Halley and the plume of the saturnian satellite Enceladus, though the question raised is to be considered very open.

The simulation results are in fact in line with what is anticipated when considering the involved grain number densities and the Debye lengths (approximated from Equation (10) in Meyer-Vernet 2013). As illustrated in Figure 8, in the 200 nm case (simulation R1 with $M^* = 1.00$), the grains are "isolated" with the intergrain distance (gray solid line) being of the same order or exceeding (for cometocentric distances exceeding 30 km) twice the Debye length (dash-dotted line). In the 2 nm case (simulation R4 with $M^* = 0.01$), the intergrain distance (black solid line) is smaller than twice the Debye length and we have a dusty plasma wherein the grains indeed play a key role in the charge balance. Figure 8 shows also that in both cases the

considered grain radii are much smaller than both the intergrain distance and the Debye length, justifying our simplification of neglecting the increase in grain-to-plasma capacitance due to neighboring grains (as discussed in Section 2.2.1).

It is our hope that the present paper will serve as motivation for the development of more detailed cometary ionospheric models incorporating (nano)grain charging. We foresee the in situ measurements by instruments on the *Rosetta* orbiter, and in relation to the present study, especially those conducted by ROSINA and instruments within the RPC near perihelion and in the innermost ionosphere. These are, for example, anticipated to reveal the dimension of the diamagnetic cavity as well as the level of electron depletion at different cometocentric distances. In addition, for ionospheric models of 67P, the in situ measurements will be of uttermost importance to set constraints on several key model input parameters (e.g., the neutral background and the electron temperature profile). This will make model–observation comparisons highly relevant as a test of our understanding of the chemical and dynamical processes at play in the innermost coma of 67P and more generally, in moderately active comets.

REFERENCES

Ågren, K., Edberg, N. T., & Wahlund, J.-E. 2012, GeoRL, 39, L10201
Balsiger, H., Altwegg, K., Bochsler, P., et al. 2007, SSRv, 128, 745
Bertaux, J.-L., Combi, M. R., Quémerais, E., et al. 2014, P&SS, 91, 14
Carr, C., Cupido, E., Lee, C. G. Y., et al. 2007, SSRv, 128, 629
Coates, A. J., Crary, F. J., Lewis, G. R., et al. 2007, GeoRL, 34, L22103
Colangeli, L., Lopez-Moreno, J. J., Palumbo, P., et al. 2007, SSRv, 128, 803
Cravens, T. E., & Körözmezey, A. 1986, P&SS, 34, 961
Davidsson, B. J. R., Gulkis, S., Alexander, C., et al. 2010, Icar, 210, 455
Draine, B. T., & Sutin, B. 1987, ApJ, 320, 803
Eriksson, A. I., Boström, R., Gill, R., et al. 2007, SSRv, 128, 729
Fink, U., & Rubin, M. 2012, Icar, 221, 721
Glassmeier, K.-H., Richter, I., Diedrich, A., et al. 2007, SSRv, 128, 649
Goertz, C. K., & Ip, W.-H. 1984, GeoRL, 11, 349
Hansen, K. C., Bagdonat, T., Motschmann, U., et al. 2007, SSRv, 128, 133
Hill, T. W., Thomsen, M. F., Tokar, R. L., et al. 2012, JGR, 117, A05209
Horányi, M. 1996, ARA&A, 34, 383
Hsu, H.-W., Horányi, M., & Kempf, S. 2013, E&PS, 65, 149
Kelley, M. S., Wooden, D. H., Tubiana, C., et al. 2009, AJ, 137, 4633
Kissel, J., Altwegg, K., Clark, B. C., et al. 2007, SSRv, 128, 823
Konno, I., Huebner, W. F., & Boice, D. C. 1993, Icar, 101, 84
Körözmezey, A., Cravens, T. E., Gombosi, T. I., et al. 1987, JGR, 92, 7331
Lara, L. M., Lin, Z.-Y., Rodrigo, R., et al. 2011, A&A, 525, A36
Larsen, T. R., Jespersen, M., Murdin, J., et al. 1972, JATP, 34, 787
Lavvas, P., Yelle, R. V., Koskinen, T., et al. 2013, PNAS, 110, 2729
Mann, I., Meyer-Vernet, I., & Czechowski, A. 2014, Phys. Rep., 536, 1
Mendis, D. A., & Horányi, M. 2013, Rev. Geophys., 51, 1
Meyer-Vernet, N. 2013, Icar, 226, 583
Morooka, M., Wahlund, J.-E., Eriksson, A. I., et al. 2011, JGR, 116, A12221
Neau, A., Al-Khalili, A., Rosén, S., et al. 2000, JCP, 113, 1762
Porco, C. C., Helfenstein, P., Thomas, P. C., et al. 2006, Sci, 311, 1393
Sagdeev, R. Z., Evlanov, E. N., Fomenkova, M. N., et al. 1989, AdSpR, 9, 263

Schleicher, D. G. 2006, Icar, 181, 442

Snodgrass, C., Tubiana, C., Bramich, D. M., et al. 2013, A&A, 557, A33

Shebanits, O., Wahlund, J.-E., Mandt, K., et al. 2013, P&SS, 84, 153

Tenishev, V., Combi, M. R., & Davidsson, B. 2008, ApJ, 685, 659

Tenishev, V., Combi, M. R., & Rubin, M. 2011, ApJ, 732, 104

Thomas, L., & Bowman, M. R. 1985, JATP, 47, 547

Trotignon, J. G., Michau, J. L., Lagoutte, D., et al. 2007, SSRv, 128, 713

Tozzi, G. P., Patriachi, P., Boehnhardt, H., et al. 2011, A&A, 531, 54

Utteback, N. G., & Kissel, J. 1990, ApJ, 100, 1315

Vigren, E., & Galand, M. 2013, ApJ, 772, 33

Vincent, J.-B., Lara, L. M., Tozzi, G. P., Lin, Z.-Y., & Sierks, H. 2013, A&A, 549, A121

Wahlund, J.-E., André, M., Eriksson, A. I. E., et al. 2009, P&SS, 57, 1795

Wahlund, J.-E., Boström, R., Gustafsson, G., et al. 2005, GeoRL, 32, L20S09

Weingartner, J. C., & Draine, B. T. 2001, ApJS, 134, 263

Wellbrock, A., Coates, A. J., Jones, G. H., Lewis, G. R., & Waite, J. H. 2013, GeoRL, 40, 4481

Whipple, E. C., Northrop, T. G., & Mendis, D. A. 1985, JGR, 90, 7405